

Energy Harvesting and Magneto-Inductive Communications with Molecular Magnets on Vibrating Graphene and Biomedical Applications in the Kilohertz to Terahertz Band

Burhan Gulbahar, *Senior Member, IEEE*

Abstract—Magneto-inductive (MI) Terahertz (THz) wireless channels provide significant theoretical performances for MI communications (MIC) and wireless power transmission (WPT) in nanoscale networks. Energy harvesting (EH) and signal generation are critical for autonomous operation in challenging medium including biomedical channels. State of the art electromagnetic (EM) vibrational devices have millimeter dimensions while targeting low frequency EH without any real-time communications. In this article, graphene resonators are combined with single molecule magnets (SMMs) to realize nanoscale EH, MIC and WPT with novel modulation methods achieving simultaneous wireless information and PT (SWIPT). Unique advantages of graphene including atomic thickness, ultra-low weight, high strain and resonance frequencies in the Kilohertz to Terahertz band are combined with high and stable magnetic moments of Terbium(III) bis(phthalocyanine) SMMs. Numerical analyses provide tens of nanowatts powers and efficiencies of $10^4 W/m^3$ in acoustic and ultrasound frequencies comparable with vibrational EH devices while millimeter wave carrier generation is numerically analyzed. Proposed model and communication theoretical analysis present a practical framework for challenging applications in the near future by promising simple mechanical design. Applications include nanoscale biomedical tagging including human cells, sensing and communication for diagnosis and treatment, EH and modulation for autonomous nano-robotics, and magnetic particle imaging (MPI).

Index Terms— Single molecule magnet, graphene, energy harvesting, magnetic induction, Terahertz, nanoscale networks, acoustic, nano-robotic

I. INTRODUCTION

MAGNETO-INDUCTIVE (MI) communications (MIC) systems have significantly high theoretical performances in Terahertz (THz) regime with applications for in-body, e.g., nanoscale biomedical communication networks for in vivo systems, and for on-chip architectures, e.g., high performance three dimensional (3D) on-chip wireless communications, as discussed in [1]. In [2], a microscale radio-frequency identification (RFID) system based on near-field magnetic resonance coupling is proposed both theoretically and experimentally for detecting intracellular activities as an experimentally important validation of nanoscale MIC

systems for biomedicine. Noninvasive and autonomous signal generation for MI transceivers in wideband spectrum including millimeter wave (mmWave) and THz bands is an important challenge. There is currently no practical and low complexity nanoscale solution for generating and modulating high frequency MI carrier signals with simple architectures in combination with energy harvesting (EH) and wireless power transfer (WPT). Single molecule magnets (SMMs) with quantum phenomena at low temperatures while having large orbital moment and magnetic stability at high temperatures are candidates for simple and high performance building blocks of nanoscale MIC [3]. SMMs have important applications including hybrid molecular spintronic devices with graphene in [3], high density information storage and quantum computing [4]. In this article, unique properties of graphene-SMM hybrid device with SMMs grafted on vibrating graphene are, for the first time, utilized for nanoscale EH, MIC and WPT by exploiting molecular dimensions, atomic thickness layering, ultra-low weight and wideband spectrum in a simple mechanical design while providing nanoscale simultaneous wireless information and power transfer (SWIPT) in the KHz to THz band.

Graphene nano-electromechanical systems (NEMS) are promising with nanoscale dimensions, high stability and operation frequencies reaching tens of GHz while electrostatic graphene microphone covers 20 Hz to 0.5 MHz band [5]. Graphene resonators or oscillators are theoretically capable of THz resonance frequencies. They have exceptional properties resulting in high performance such as large Young's modulus (1 TPa for single layer graphene (SLG)), low residual stress and large breaking strength (allowing 25% strain level) for strong and durable devices and ultra-low weight for utilization in challenging medium such as for biological applications [6]. In this article, they are utilized for MI signal generation in combination with grafted SMMs. Graphene-SMM hybrids preserve magnetic properties of SMM Terbium(III) bis(phthalocyanine) ($TbPc_2$), i.e., a single Tb (III) ion sandwiched between two planar phthalocyanine (Pc) ligands, and graphene, based on similar hybrid architectures realized with carbon nanotubes (CNTs) and graphene [3], [7], [8], [9]. Proposed system is applicable for other kinds of SMMs preserving magnetic properties in contact with graphene. Properties of CNT-SMM hybrid are preserved in [8] with a highly efficient grafting process. In [7], static magnetic properties, structural and electronic properties of SMMs on graphene are not

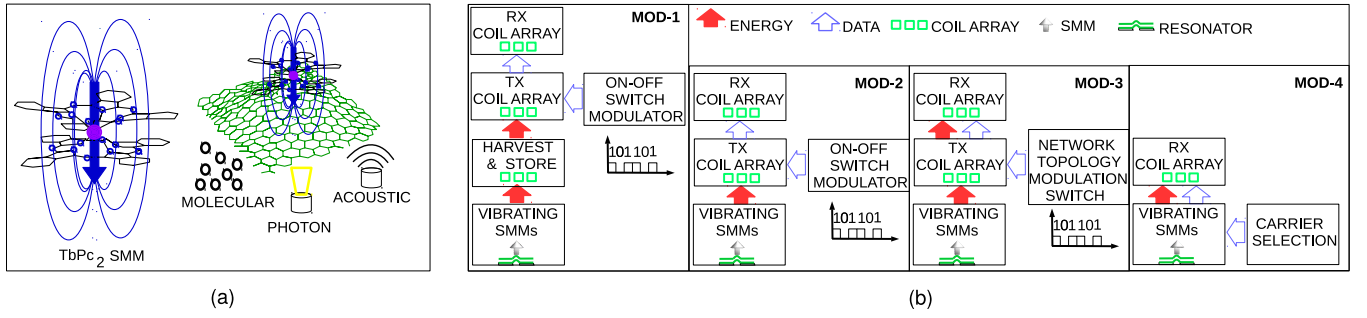


Fig. 1. (a) TbPc₂ molecular nanomagnet attached to resonating graphene sheet, and (b) four different SMM based EH modulation methods with different energy utilization, data modulation and hardware blocks of the coil units.

modified. In [10], a super lattice of SMMs (Fe₄H) is formed on graphene with magnetic easy axis of each molecule oriented perpendicular to the surface and forming a 2D array of SMMs retaining their bulk magnetic properties. Nonlinear mechanical properties of CNT are utilized in [8], [9] with frequency shift depending on applied magnetic field and magneto-mechanical effects. Graphene-SMM hybrid is, for the first time, utilized to realize MIC, EH and WPT simultaneously.

State of the art micro-magnet and micro-coil EH combinations are not designed to produce wide band and tunable frequency signals while utilizing lower frequencies with millimeter level areas not suitable for nanoscale communications, and with efficiencies smaller than 10^5 W/m^3 [11]. In [12], EH is performed from 330 MHz and 0.5 nm vibration amplitude of permanent magnet on nanoplates with an efficiency on the orders of several 10^3 W/m^3 without detailed analysis of performance scalability with respect to geometrical and magnetic characteristics of the device. On the other hand, nanoscale EH of different kinds transducing acoustic energy to electricity are future promising to provide noninvasive and continuous energy for autonomous operation [13]. However, electrostatic, piezoelectric, triboelectric, micro-fluid or magnetostrictive types harvest energy from low frequency ambient vibrations without any target for high frequency signal generation and communications. Besides that, in this article, a novel method to produce MI THz signals is proposed with a simple mechanical design as discussed in [1].

Magnetic resonance imaging (MRI) and magnetic particle imaging (MPI) are limited by the amount and the size of the particles. Resolution with superparamagnetic iron oxide nanoparticles (NPs) (SPIONs) is approximately 1 mm while promising 300 μm resolution with optimized NPs, hardware and pulses [14]. SPIONs are utilized for imaging contrast enhancement, immunoassays, tissue repair, magnetic hyperthermia and drug delivery. However, finite resolution is challenging to discriminate cells in the same area. In the proposed article, resonators can be injected into cells or their environments for carrier based tagging in MPI systems.

The contributions achieved in this article are as follows:

- (a) SMMs are utilized in a novel nanoscale MIC, EH and WPT application with a special mechanical design utilizing vibrating graphene and TbPc₂ type SMMs. The proposed system has spatial diversities of multiple SMMs,

multiple resonators and multiple layers of resonators, and with computed efficiencies by numerical analyses reaching 10^4 W/m^3 and tens of nanowatts (nWs) peak powers in acoustic and ultrasound frequencies.

- (b) Modulation mechanisms are proposed for nanoscale MIC with EH resonators and network topology modulation method introduced in [15] for SWIPT.
- (c) Design of a simple, mechanical and EH tagging method is presented for nanoscale and microscale size units. Future applications include tagging biological structures such as human cells by utilizing frequency diversity and hundreds of micrometers communication ranges which can be extended to millimeter and centimeter scales with passive waveguides in [1] promising a novel monitoring, target tracking and cellular level MPI system.
- (d) A system design is proposed to generate mmWave and THz carrier waves to be utilized in low power and high frequency on-chip and in-body MIC and WPT applications while promising optimizations in future works such as receiver diversity with multiple carriers.

The remainder of the paper is organized as follows. In Section II, we present the hybrid graphene-SMM device structure. Then, in Section III, EH and MIC device models are presented for small radius and large radius resonators. In Section IV, the channel models for diversity combining architectures are presented. Then, in Section V, experimental challenges are discussed while potential applications are discussed in Section VI. Numerical analyses for varying geometrical parameters are performed in VII. Finally, Section VIII concludes the paper.

II. GRAPHENE-SMM RESONATOR BASED MODULATION METHODS

Terbium ion molecules are attached on graphene resonator as shown in Fig. 1(a) similar to the architectures proposed for CNTs in [8] and [9] in terms of the mechanical design. SMMs on vibrating graphene create an oscillating magnetic field which is utilized for inducing currents in a nearby receiver coil based on Faraday's law of induction for MIC, EH and WPT purposes. In [8], a highly efficient grafting process of TbPc₂ SMMs onto a CNT NEMS is proposed while it is highly sensitive even at a molecular magnet level. Superlattices of single atom magnets on graphene are realized with a density of 115 Tbit/inch² promising high density structures in [16].

TABLE I
GRAPHENE AS EXCITATION SOURCE OR UNDER PRESSURE

Device	Excitation Source	Under Pressure	Mechanism	Max. Freq.
Phonon Laser [24]	Acoustic modulator	-	Cerenkov emission	10 THz
Modulator [25]	Optical modulator	-	Plasmonic hybrid electro-optic	Tens of THz
Microphone [17]	-	Sound Pressure	Air molecules	500 KHz
Resonator [18]	-	Electrostatic pressure	Back-gate voltage	178 MHz
Strained graphene [19]	-	Optical pressure	Optical force	-
Strained graphene [20]	-	Molecular pressure	Gas molecules	-

Grafting methods allow high density graphene-SMM hybrid design [8], [10], [16].

Graphene resonators are modulated with varying sources, e.g., acoustic [17], electrostatic [18], optical [19], mechanical strain or molecular forces [20], as shown in Table I. Examples are provided for both the cases where the graphene is utilized as a *source* of acoustic or optical signals for creating external excitation, and where it is modulated as a *resonator under pressure* by external excitation. Hundreds of MHz modulation frequencies are experimentally realized on graphene resonators while there is a diversity of methods for specific applications. Tens of THz optical or acoustical modulations are possible by utilizing graphene sources for an *all-graphene system design* with simplified manufacturing. However, special design is necessary to utilize the force produced by graphene sources on graphene resonators as an open issue.

Theoretical model for resonators is based on experimentally verified models summarized in [6]. Resonators are clamped circular plates realized with graphene and mechanical motion is modeled using plate theory as emphasized in [6], [21]. Harmonic oscillator equation with a forced oscillation of uniform pressure $P_g \cos(\omega_0 t)$ and force $F_g = P_g \pi r_g^2 \cos(\omega_0 t)$ is utilized where $\omega_0 = 2\pi f_0$ is the resonance frequency and r_g is the radius of the resonator. Steady-state resonance amplitude (d_0) at the center for the first mode of resonance is approximated by assuming plate model (thick resonators) and using equations (16) and (22) in [22] as follows:

$$d_0 = \frac{2\pi P_g r_g}{\rho h_g N_1} \frac{\Gamma_{\alpha, r_g} (1 - \Lambda_{\alpha, r_g})}{\omega_0^2 \sqrt{(1 - (\frac{\omega}{\omega_0})^2)^2 + 4\zeta^2 (\frac{\omega}{\omega_0})^2}} \quad (1)$$

where $\Gamma_{\alpha, r_g} = \alpha^{-1} (J_1(\alpha r_g) - \Lambda_{\alpha, r_g} I_1(\alpha r_g))$, $\Lambda_{\alpha, r_g} = J_0(\alpha r_g) / I_0(\alpha r_g)$, $J_o(\cdot)$ and $I_o(\cdot)$ are the Bessel and modified Bessel functions of first kind and order o for $o \in [0, 1]$, respectively, $N_1 = \int_0^{r_g} 2\pi r W^2(r, \theta) dr$, $W(r, \theta) = J_0(\alpha r) - \Lambda_{\alpha, r_g} I_0(\alpha r)$, αr_g changes between 2.404 and 3.196 transforming from membrane to the plate type as shown in Fig. 2 of [6], $\sqrt{r_g^2 T_g / D}$ is the transition variable denoted by k in [22], $D = E h_g^3 / (12(1 - v^2))$ is the flexural rigidity, T_g is the pretension in (N/m), ρ is 3D mass density, v is the Poisson's ratio, E is the Young's Modulus, h_g is the resonator thickness, μ_m is the damping coefficient (kg/s) of the medium and ζ depending on ρ , h_g , ω_0 and μ_m [23]. Although detailed modeling of d_0 is available in [22], analytical calculations for d_0 is simplified with strain based modeling. Assume that deflection at the radial position r is given as $d_0 (1 - r^2 / r_g^2)$ with a parabolic approximation of the shape.

Then, percentage of strain denoted by S_m is approximated as $S_m / 100 = (2 d_0^2) / (3 r_g^2) - (2 d_0^4) / (5 r_g^4)$ for small strain levels. Graphene is highly strong tolerating strain levels of as much as 25% [26]. Performance is measured with respect to a specific level of strain. Detailed analysis for the dependence of strain on the applied force is provided in detail in [23] where acoustic forces are utilized in varying medium.

Resonance frequencies (f_0) for SLG and multi-layer graphene (MLG) are calculated with experimentally verified plate and membrane models in (8) and (9) in [6] as follows:

$$f_{0,SLG} = \frac{2.404}{2\pi r_g} \sqrt{\frac{T_g}{h_g \rho}} \quad (2)$$

$$f_{0,MLG} = \sqrt{f_{0,SLG}^2 + \left(\frac{10.21}{4\pi} \sqrt{\frac{E}{3\rho(1-v^2)}} \frac{h_g}{r_g^2} \right)^2} \quad (3)$$

It is assumed that magnetic moments of SMMs are aligned in parallel with the external magnetic field leading to zero magnetic torque compared with magnetometer structures in [8], [9]. Therefore, SMMs behave as loads on resonating layer without changing magnetic and structural properties of SMM and graphene with methods in [7], [8], [9], [10], [16]. The change in f_0 of graphene layer is approximated in [21] by $|\partial f| = f_0 |\partial m| / (2m)$ where m is the resonator mass and $|\partial m|$ is the load leading to $|\partial f| = f_0 m_{M,SMM} / (2m_G)$ where $m_G = \rho h_g \pi r_g^2$ and $m_{M,SMM} = N_{SMM} m_{SMM}$ are the weights of resonator and SMMs grafted on it, respectively, N_{SMM} is the number of SMMs and m_{SMM} is the weight of each SMM. N_{SMM} is chosen small for the minor effects on resonance, i.e., $m_{M,SMM} = \eta_{SMM} m_G$ where $\eta_{SMM} \ll 1$.

In Table II and Fig. 1(b), four different modulation methods are proposed where energy is harvested from graphene-SMM resonators. Mod-1 stores harvested energy and utilizes later. Microscale coils in [1] utilize 1 μ W transmit (Tx) power to achieve THz communications and this energy can be stored in several minutes with the efficiency of ≈ 1 nW, resonator radius of 50 μ m and coil radius of 5 μ m as discussed in Section VII. Mod-2 utilizes real-time simultaneous energy harvesting and data modulation by switching the coil ON and OFF and modulating harvested carrier signal. Mod-3 utilizes network topology modulation defined in [15] for SWIPT by modulating array of active coils and by utilizing real-time harvested energy without any signal modulation. Mod-4 transmits carrier signal directly without any Tx coil while receiver (Rx) estimates the frequency for tagging purposes. In this study, Mod-1 for EH and Mod-4 for tagging are analyzed while the others are open

TABLE II
SMM BASED DATA AND ENERGY MODULATION METHODS

ID	SMM Utilization in Tx	Energy Storage in Tx	Transmit Power Limit	SWIPT	Data Modulation
Mod-1	Harvesting	√	Battery	-	ON-OFF Keying [1]
Mod-2	Oscillator	-	MI channel (SMM to Tx)	-	ON-OFF Keying [1]
Mod-3	Oscillator	-	MI channel (SMM to Tx)	√	Network Topology Mod. [15]
Mod-4	Tagging	-	MI channel (SMM to Rx)	√	Carrier Selection

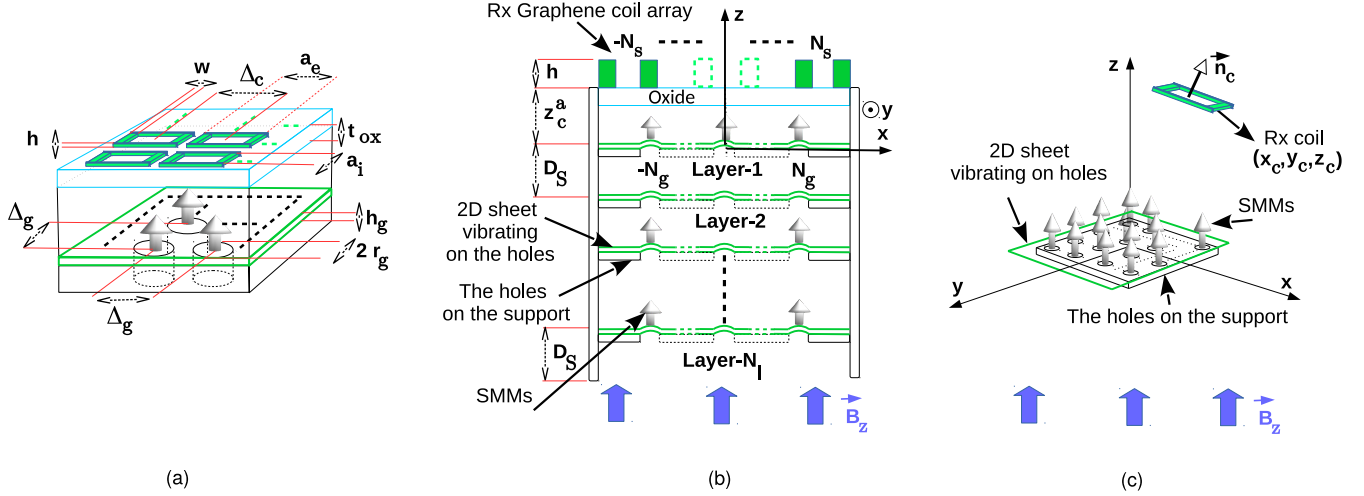


Fig. 2. EH device geometries for the types of (a) SLMO, (b) MLMO, and (c) the system model for SMM based wireless communications channel where the coil resides at (x_c, y_c, z_c) with the normal vector of \hat{n}_c .

issues. Next, SMM magnetic moment modeling are presented by emphasizing the relation with the graphene surface and relaxation.

A. SMM Spin Orientation and Relaxation Modeling

In this article, it is assumed that the proposed device operates at room temperature. Magnetic moments of SMMs are assumed to be aligned with an external magnetic field while optimum system design and engineering of external fields and SMM orientations are open issues. In addition, it is assumed that magnetic easy axis of each SMM molecule is oriented perpendicular to the graphene vibrator as discussed in [10] and there is no magnetic torque applied on graphene due to misalignment between SMM moment and external field as in [8], [9]. The effects of misalignments resulting in frequency shift are left as future works.

On the other hand, graphene-SMM hybrid vibration promises relaxation based analysis similar to MPI [14]. Relaxation time at high temperatures is given by Arrhenius equation with $\tau_N = \tau_0 e^{\Delta/k_B T}$ where Δ is the anisotropy barrier given as 566 cm^{-1} for TbPc_2 SMM and assuming $\tau_0 = 10^{-9}$ seconds [27], and k_B is approximately $0.695 \text{ cm}^{-1}/\text{K}$. Room temperature ($k_B T \approx 200 \text{ cm}^{-1}$) results in $\tau_N \approx 15.1 \text{ ns}$ with $1/\tau_N \approx 66 \text{ MHz}$. Future studies utilizing the proposed resonator at room temperature are limited by relaxation time on the order of tens of nanoseconds. Mechanisms to exploit the proposed system for MPI purposes are left as future works. Next, modulator device architecture is modeled by providing analytical formulation of inductive channel.

III. MAGNETO-INDUCTIVE MODULATOR MODELING

Oscillators are placed on a grid of holes, and coils induced by vibrations are placed in a multi-receiver architecture. Device geometries for EH purposes with single layer (SL) multiple oscillator (MO) and multiple layer (ML) MO abbreviated as SLMO and MLMO, respectively, are shown in Figs. 2(a) and (b), respectively. Single resonator case is denoted with SLMO. EH device is realized with closely and vertically separated, and parallel oriented hybrid structures while MIC design is shown in Fig. 2(c) where Rx coil resides at (x_c, y_c, z_c) with the normal vector \hat{n}_c . The center of resonators is positioned at the origin of the reference system. $\Delta_g = (k_{\Delta_g} + 2)r_g$ and $\Delta_c = (k_{\Delta_c} + 2)a_e$ denote the central distances of SOs and coils, respectively, where k_{Δ_g} and k_{Δ_c} are constant separation factors. Inner and outside lengths of coils are a_i and a_e , respectively, where they are determined with respect to the width (w) and the height (h) of the coil wire with $a_i = 2 \times k_w \times w$, $a_e = a_i + 2 \times w$, k_w is a constant and $w = h$ with a square cross section. Coil resides on an oxide substrate with a thickness of t_{ox} with circuit model presented in Appendix as a simple device model to characterize the approximate performance.

Distance of the first layer of SMM oscillators to the bottom of the coil (neglecting oxide thickness much smaller than h) is denoted with z_c^a where z-axis position of the central coordinate of coil is found by $z_c = z_c^a + h/2$. D_S denotes the thickness of a SL calculated by allowing phase synchronization errors between different layers as shown in Fig. 3. The maximum number of layers is assumed to be limited by N_l . The layer thickness is assumed to be equivalent

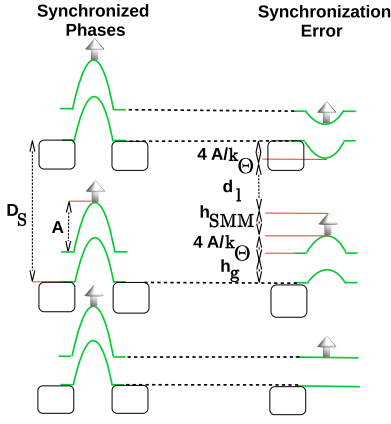


Fig. 3. The effect of the synchronization error in MLMO resonators and the calculation of D_S .

to $D_S \equiv d_l + h_M + h_g + 8A/k_\theta$ where d_l is the inter-layer separation distance, A is the vibration amplitude, h_M denotes the height of the SMM cluster on the resonator (on the order of nms) and $k_\theta \gg 1$ is the tolerance factor to the phase errors due to excitation sources or other mechanical effects. It is assumed that the total thickness of the layers is limited by $D_T^{max} \equiv \lambda_e/k_\theta$ where $\lambda_e = v_e/f_0$ is the excitation signal wavelength and v_e is the velocity of the excitation signal. The worst synchronization error is tolerated with a distance between the layers, i.e., $1/k_\theta$ multiplied by the total distance that the SMMs in two consecutive layers vibrate which is $2 \times 4 \times A$. Then, $N_l \leq D_T^{max}/D_S$ where $2 \times N_s + 1$ and $2 \times N_g + 1$ denote the numbers of Rx coils and resonators in a row, respectively, with a square grid placement as shown in Figs. 2(a) and (b). Static magnetic field is assumed to be in the z axis with the value \vec{B}_z while a scanning device can be utilized to find the best orientation in practice. Next, architectures denoted as Sch-1 and Sch-2 are described improving the geometry in Fig. 2(b).

A. Scheme-1 Device Geometry

In Sch-1, the dimension of each SO is assumed to be very small compared with the dimension of the coil such that a large number of resonators is placed under the coil especially for EH or carrier generation. Geometries of holes and coils are shown in Figs. 4(a) and (b), respectively, where the total area is a circular region with radius determined by $(N_s + 1)\Delta_c$, and N_s this time denotes the number of circularly placed layers of coils as different from Fig. 2(b). Coils are more compactly placed compared with the square grid structure. Assuming rotational symmetry of the induction, induced voltage is calculated by grouping SOs with respect to the distance to the coil centers. This lowers the complexity due to double integrations in formulations in Section IV for each pair of the coils and the resonators. Total area of resonators is compatible with the total area of coils such that total number of SOs is approximated by $\pi(N_s + 1)^2 \Delta_c^2 / \Delta_g^2$. The angle between radial lines connecting two neighbor coils on j th circle with the radius of $j\Delta_c$ is set to $\Psi(j) = \cos^{-1}(1 - 0.5/(j-1)^2)$ for $j \geq 2$, and $j = 1$ denotes a single coil case with $\Psi(1) \equiv 2\pi$

and $N_s = 0$. Total number of coils is given approximately by $N_{coil} = \sum_{i=1}^{N_s+1} 2\pi/\Psi(i)$.

B. Scheme-2 Device Geometry

In Sch-2, larger resonators comparable with coils are utilized, and a square grid based placement is realized as shown in Figs. 4(c) and (d). Resonators and coils are placed at positions $[m\Delta_g, n\Delta_g, 0]$ for $m, n \in [-N_g, N_g]$ and $[m\Delta_c, n\Delta_c, z_c]$ for $m, n \in [-N_s, N_s]$, respectively, with a total of $(2N_g + 1)^2$ resonators and $(2N_s + 1)^2$ coils, respectively. N_g is chosen in compatible with total area of coil array with the formulation for rounded integer values of $N_g \approx (N_s + 1/2)\Delta_c/\Delta_g - 1/2$. Next, induction channels between SMMs and coils are modeled.

IV. WIRELESS CHANNEL MODEL

MI channels for SLSO, SLMO and MLMO cases are modeled consecutively. Magnetic dipole moment (\vec{m}) amplitude of Tb ion is calculated by $g_J \mu_B J$ where $g_J = 1.326$ is Lande g-factor, $J = 6$ is the total angular momentum quantum number and $\mu_B = 9.27 \times 10^{-24}$ J/T is Bohr magneton [8]. Next, Faraday's law of induction is used for produced dipole field.

A. Single SMM to Single Coil Wireless Channel

Magnetic induction of a single SMM dipole on a rectangular coil is modeled as follows. Flux $\Phi_{z,u}$ through a square area of side lengths u at \vec{z} is approximated as $\Phi_{z,u} = \int_{-u}^u \int_{-u}^u \vec{B} \cdot \vec{n}_c d\tilde{x} d\tilde{y}$ where $(\tilde{x}, \tilde{y}, \tilde{z})$ is the local coordinate system of the square with the coinciding center, sides of the rectangle are parallel with \tilde{x} and \tilde{y} axes, \vec{B} is the magnetic field along the area of region, and \vec{n}_c is the normal vector of the square area as shown in Fig. 2(c). Assume that coil center is at $\vec{s}_c = [x_c, y_c, z_c]$. Then, generated field due to a single SMM of the moment \vec{m} is found by modifying the equations (2) and (3) in [28] with the randomly oriented coil as follows:

$$\vec{B} = \frac{\mu_0 |\vec{m}|}{4\pi} \frac{3xz\vec{e}_x + 3yz\vec{e}_y - (r^2 - 2z^2)\vec{e}_z}{(r^2 + z^2)^{5/2}} \quad (4)$$

where \vec{e}_x , \vec{e}_y and \vec{e}_z are unit vectors of the Cartesian coordinate system (x, y, z) that SMM resides as shown in Fig. 2(c), $\{r, x, y, z\}$ are functions of $(\tilde{x}, \tilde{y}, \tilde{z})$ such that $r = \sqrt{x^2 + y^2}$ and $[xyz]^T = \vec{s}_c + \tilde{x}\vec{e}_x + \tilde{y}\vec{e}_y + \tilde{z}\vec{n}_c$ where \vec{e}_x and \vec{e}_y are unit vectors on the plane of the square coil in local coordinate system. If SMM vibration has a sinusoidal form then, $z_c(t) = z_c + A \sin(\omega_0 t)$. Then, total flux through coil becomes $\Phi(t) = F_c N_T (1/A_c) \int_{-h/2}^{h/2} \int_{-u}^u \Phi_{z,u} du d\tilde{z}$ where $F_c = N_T A_s/A_c$ is the fill-factor, A_s and $A_c = w \times h$ are the areas of the coil cross-sections of single turn and total coil device, respectively, and N_T is the number of turns. Induced voltage $V_S(t) \equiv -d\Phi(t)/dt$ on the coil is found by using $-d\vec{B}/dt$ as follows:

$$V_S(t) = \vec{m} \dot{z} \int_{a_i}^{a_e} \int_{-h/2}^{h/2} \frac{\partial \Phi_{z,u}^n}{\partial z} d\tilde{z} du \quad (5)$$

where $\Phi_{z,u}^n$ is the normalized flux with unity $|\vec{m}|$ in (4), $\vec{m} \equiv \mu_0 |\vec{m}| F_c N_T / (4\pi A_c)$, $\dot{z} = \dot{z}_c(t) = -dz/dt$ and

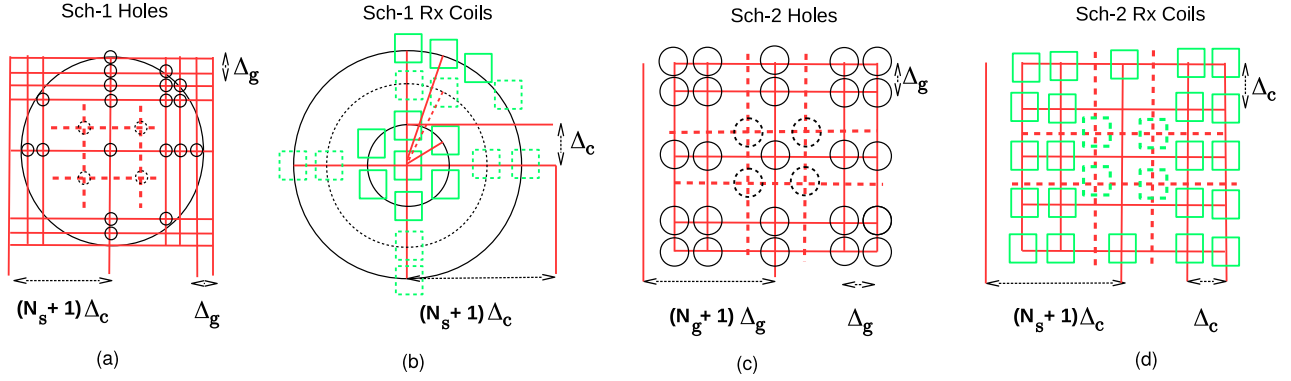


Fig. 4. The geometries of (a) the holes and (b) the coils in Sch-1, and (c) the holes and (d) and the coils in Sch-2 device types.

$\mu_0 = 4\pi \cdot 10^{-7}$ (T \times m/A) is the vacuum permeability. Expression is simplified with assumptions about the coil orientation and that rotating rectangular coil around its central axis does not change the induction significantly. If $\vec{n}_c = \vec{e}_z$, $y_c = 0$, $r_c = x_c$, $\vec{e}_{\tilde{x}} = [1\ 0\ 0]$ and $\vec{e}_{\tilde{y}} = [0\ 1\ 0]$, then $\Phi_{z,u}^n$ becomes $2u(\zeta_+\chi_+ + \zeta_-\chi_-)/(\zeta_-\zeta_+ + \rho)$ where $\zeta_{\pm} = \sqrt{\Upsilon_{\pm} + u^2}$, $\Upsilon_{\pm} = \gamma_{\pm} + \beta$, $\beta = (z_c + \tilde{z})^2$, $\gamma_{\pm} = (u \pm x_c)^2$, $\chi_{\pm} = \Upsilon_{\pm}(u \mp x_c)(\gamma_{\mp} + 2\beta + u^2)$ and $\rho = \Upsilon_- \Upsilon_+ (\beta + u^2)$. Then, $(-1/2u) \partial \Phi_{z,u}^n / \partial z$ is found as follows:

$$\begin{aligned} & \frac{\rho \zeta_+^2 \chi_+ + \frac{\partial \zeta_-}{\partial z_c} \zeta_- \zeta_+ + \frac{\partial \rho}{\partial z_c} (\zeta_- \chi_- + \zeta_+ \chi_+)}{\zeta_-^2 \zeta_+^2 \rho^2} \\ & + \frac{\rho \zeta_- \left(\zeta_- \chi_- - \frac{\partial \zeta_+}{\partial z_c} \zeta_+ - \zeta_+ \left(\zeta_- \frac{\partial \chi_-}{\partial z_c} + \zeta_+ \frac{\partial \chi_+}{\partial z_c} \right) \right)}{\zeta_-^2 \zeta_+^2 \rho^2} \end{aligned} \quad (6)$$

where derivatives are $\partial \zeta_{\pm} / \partial z_c = \sqrt{\beta} / (\sqrt{\Upsilon_{\pm} + u^2})$, $\partial \chi_{\pm} / \partial z_c = 4\sqrt{\gamma_{\mp} \beta} \Upsilon_{\pm} + 2\sqrt{\gamma_{\mp} \beta} \times (\gamma_{\mp} + 2\beta + u^2)$ and $\partial \rho / \partial z_c = 2\sqrt{\beta}((\beta + u^2)(\Upsilon_+ + \Upsilon_-) + \Upsilon_- \Upsilon_+)$. The maximum amplitude of the generated voltage is calculated by inserting $\tilde{z} = A \cos(\omega_0 t) \omega_0$ into (5) resulting in the value denoted by $|V_i| \equiv \max\{|V_S(t)|\}$. If SMMs are positioned at the center of the coordinate frame on the xy plane, then V_i on the coil at (x_c, y_c, z_c) is given as follows:

$$V_i = A \omega_0 \overline{n} \int_{a_i}^{a_e} \int_{-\frac{h}{2}}^{\frac{h}{2}} \frac{\partial \Phi_{z,u}^n}{\partial z} d\tilde{z} du \quad (7)$$

while depending on z_c and $r_c = \sqrt{x_c^2 + y_c^2}$. Multiple SMMs are used for diversity next.

B. Diversity Combining with Multiple SMMs

Induced voltage is improved with collective moments of a group of SMMs. Their relative positions are assumed the same since they are placed in an area of radius $k_r r_g$ where $k_r \ll 1$ for large r_g while SMMs placed in a compact manner to the center for r_g near several nanometers. As discussed in Section II, ratio of the total weight of the SMMs to the weight of 2D layer is η_{SMM} with an overall effect of the frequency shift to $(1 - \eta_{SMM}/2) \times f_0$. Then, the height of the total group of SMMs is roughly estimated as $h_M = h_{SMM} \max\{N_{SMM} / (\pi (k_r r_g)^2 / a_{SMM}^2), 1\}$ where

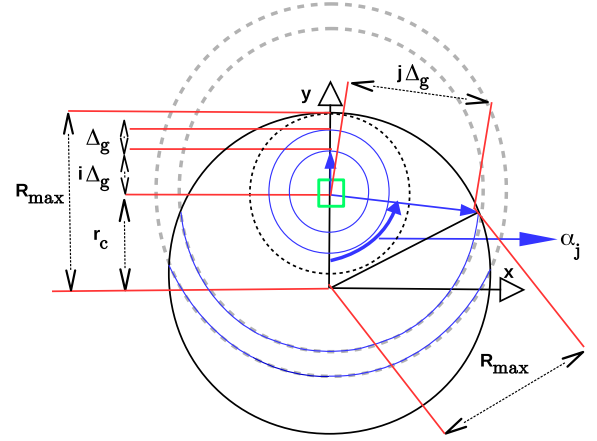


Fig. 5. The geometry for the calculation of the induced voltage in Sch-1 case for $r_c \leq R_{max}$ case.

a_{SMM} is the side length of the placement square for a single SMM and h_{SMM} is its height. The resulting V_i is denoted by V_{z_c, r_c}^{SLSO} . Next, multiple SOs are utilized to form SLMO.

C. Diversity Combining with Multiple Oscillators

Total V_i for Sch-1 on a coil at radial and vertical distances r_c and z_c , respectively, is denoted by V_{z_c, r_c}^{SLMOc} where calculation method and geometry are shown in Fig. 5 for $r_c \leq R_{max}$ with the arcs for two different regions while radius of total area is $R_{max} \equiv (N_s + 1) \Delta_c$, $r_d \equiv R_{max} - r_c$ and each SO with an area of $\approx \Delta_g^2$. It is approximated for $r_c \leq R_{max}$ as follows:

$$\begin{aligned} V_{z_c, r_c}^{SLMOc} \approx & \sum_{i=0}^{\lfloor r_d / \Delta_g \rfloor} \Gamma_n C(i) V_{z_c, i \Delta_g}^{SLSO} \\ & + \sum_{j=\lfloor r_d / \Delta_g \rfloor + 1}^{\lfloor (2R_{max} - r_d) / \Delta_g \rfloor} (\Gamma_n \alpha_j / \pi) C(j) V_{z_c, j \Delta_g}^{SLSO} \end{aligned} \quad (8)$$

where $\lfloor \cdot \rfloor$ is the floor function and $\alpha_j = \cos^{-1}(-(R_{max}^2 - r_c^2 - j^2 \Delta_g^2) / (2r_c j \Delta_g))$ gives the proportional angle of the arc to calculate its area while if $r_c > R_{max}$, the approximation becomes $V_{z_c, r_c}^{SLMOc} \approx \sum_{i=i_s}^{i_e} (\Gamma_n \alpha_i / \pi) C(i) V_{z_c, i \Delta_g}^{SLSO}$ where $i_s = \lfloor (r_c - R_{max}) / (\Delta_g) \rfloor + 1$, $i_e = \lfloor (r_c + R_{max}) / (\Delta_g) \rfloor$, and $C(i) = \pi((i+1)^2 - i^2)$ is the approximate number

of SOs in the arc area where radial distance of the coil to the resonators in the circular area between the indices i and $i + 1$ becomes $\approx i \Delta_g$. Result is normalized by $\Gamma_n \equiv (\pi R_{max}^2 / \Delta_g^2) / \sum_i C(i)$. In Sch-2, V_i denoted by $V_{z_c, i_x, i_y}^{SLMOr}$ in the coil at $[i_x \Delta_c, i_y \Delta_c, z_c]$ is approximated as follows:

$$V_{z_c, i_x, i_y}^{SLMOr} \approx \sum_{m=-N_g}^{N_g} \sum_{n=-N_g}^{N_g} V_{z_c, r_c(i_x, i_y, m, n)}^{SLSO} \quad (9)$$

where $r_c(i_x, i_y, m, n) = \sqrt{\varsigma_{m, i_x}^2 + \varsigma_{n, i_y}^2}$ between each SO and the coil, and $\varsigma_{i,j} \equiv i \Delta_g - j \Delta_c$.

D. Diversity Combining with Multiple Layers

Total voltage values for Sch-1 and Sch-2 cases are given by the following, respectively:

$$V_{z_c, r_c}^{MLMOc} = \sum_{i=1}^{N_l^*} V_{z_c + (i-1) D_S, r_c}^{SLMOc} \quad (10)$$

$$V_{z_c, i_x, i_y}^{MLMOr} = \sum_{i=1}^{N_l^*} V_{z_c + (i-1) D_S, i_x, i_y}^{SLMOr} \quad (11)$$

where distance of i th layer to the coil is given by $z_c + (i - 1) D_S$ and N_l^* is found by either maximizing the volumetric energy efficiency of EH device or maximizing the received power P_h for single device unit. Number of layers is limited by $N_l = \min\{D_T^{max} / D_S, D_{max} / D_S\}$ where $D_T^{max} = \lambda_e / k_\Theta$ and D_{max} is the application specific EH device height, e.g., bounded by the biological unit that the coil to be placed. The number of layers is optimized as follows:

$$\max P_h / (z_c^a + w + N_l^* D_S) \text{ s.t. } N_l^* \leq N_l \quad (12)$$

where resulting device has the highest volumetric EH efficiency computed with $Eff_h = P_h / V_r$ in (W/m^3) in a single coil and device volume V_r is approximated by $A_r \times h_r \approx A_r \times (w + N_l D_S)$ for $z_c^a \ll 1$. Device area values (A_r) for the two schemes are A_C and $\max\{A_C, (2 N_g + 1)^2 \Delta_g^2\}$ while A_C equals to $\pi (N_s + 1)^2 \Delta_c^2$ and $(2 N_s + 1)^2 \Delta_c^2$, for Sch-1 and Sch-2, respectively.

V. EXPERIMENTAL CHALLENGES AND ANALYSIS OF MODELING ACCURACY

There is a set of challenges to be solved for realizing prototype. Fundamental idea, i.e., EH from SMMs on vibrating 2D planes (such as black phosphorus and transition metal dichalcogenides (TMDCs) including molybdenum disulfide (MoS_2) in addition to graphene) and utilizing for MIC and WPT allow different architectures to be designed specific to the application. Therefore, specific analysis and experimental verification methods are necessary. Next, potential sources of error in modeling and realization are discussed. Then, finite element method (FEM) based simulation to improve accuracy for complicated geometries and importance of experimental measurements to improve analytical models are discussed. Issues regarding manufacturing and geometrical design, toxicology and operation in biological environments are discussed.

A. Modeling Accuracy Analysis

There are approximations in analytical models requiring experimental feedback. Different types of resonators in literature have varying performances specific to each design as listed in [6]. Potential sources of error requiring experimental feedback are summarized as follows:

- Effect of SMMs on vibration should be experimentally analyzed in terms of frequency shift where the model in [21] is utilized, i.e., $|\partial f| = f_0 |\partial m| / (2 m)$.
- Vibration properties in THz regime in terms of hybrid design and hole geometry should be experimentally determined for an improved model for high frequencies.
- Placement of multiple SMMs in a small area on resonator and the distribution of their easy axes should be experimentally modeled while perpendicular and homogeneous distribution is assumed based on advanced grafting methods in [10], [16]. Effect of vibration on the distribution and total magnetic moment should be experimented.
- Effects of external magnetic field in arbitrary angles should be modeled in terms of the generated torque on SMMs and their effect on vibration.
- Receiver coil design should be optimized based on the detailed model in [1] and modeling accuracy should be improved by simulation and experimental studies.
- Steady state and transient response characteristics should be experimentally measured to model non-linear and unplanned effects of the environment and hybrid design.
- It is assumed that multiple layers of resonators are placed in an ordered manner by using advanced manufacturing methods such as carbon nanomembranes (CNMs) as discussed in [29] for a similar multi-layer architecture with vibrating quantum dots (QDs). Modeling errors in terms of vibrational properties in such a design should be experimentally determined.

B. FEM Simulations and Experimental Verification

Theoretical analysis is based on experimentally verified models of resonators in [6], [21], magnetic characteristics of graphene-SMM hybrid in [8], [7], [10] and inductive coupling of a magnetic particle with a circular coil in [28]. Furthermore, proposed models form the first step of any FEM simulation, i.e., mathematical modeling. In addition, we simplify device geometry with the architecture in Fig. 4 and provide discretization methods of calculation in Fig. 5. Since the set-up is simple as composed of resonators with magnetic particles and circular coils, numerical analysis without FEM based discretization is a good approximation compared with FEM simulations used for complicated systems. However, proposed designs should be simulated with FEM tools and experimentally measured to improve the analytical model and to accurately model nonlinear effects in terms of deflection, multi-layer design and interactions with SMMs.

Resonator is assumed to be oscillating periodically without nonlinear terms at higher bands. Performance degradation with nonlinear carrier signals due to mechanical effects, SMM mass, rotational or similar complicated mechanisms should

TABLE III
NUMERICAL ANALYSIS PARAMETERS

PARAMETER	VALUES	PARAMETER	VALUES
μ_B	$9.27 \cdot 10^{-24}$ (J/T)	m_{SMM}	$2 \cdot 10^{-21}$ (gr)
J	6	h_{SMM}	0.35 (nm)
g_J	1.326	a_{SMM}	1.5 (nm)
k_B	$1.38 \cdot 10^{-23}$ (J/K)	η_{SMM}	0.1
ρ	2200 (kg/m ³)	r_g	3 nm - 150 μ m
v	≈ 0.16	k_r	0.2
E	1 (TPa)	$k_{\Delta c}, k_{\Delta g}$	1
T	300 (K)	T_g	0.1 (N/m)
N_T, N_s	1, 0	k_Θ	36, 180, 360, 1800
t_{ox}	300 (nm)	S_m (%)	10^{-4} , 1, 20
$w = h$	5, 10, 50 (μ m)	d_l	10^{-9} , 10^{-7} , 10^{-6} (m)
k_w	0.1	ρ_c	10^{-12} (Ω m ²)

be theoretically modeled, numerically simulated and experimentally determined. Synchronization between layers and performance of varying sets of excitation sources should be experimented. Storage of harvested energy for Mod-1 should be designed with high efficiency by analyzing state of the art supercapacitive devices. Furthermore, methods should be developed to stack multiple layers with nanoscale precision.

C. Toxicology and Effects of Biological Environments

Toxicology of graphene is discussed in detail in [1] where various encapsulation methods and studies on the effects of graphene on organs are discussed. Graphene is promising as a bio-compatible device. Terbium compounds have low to moderate toxicity, however effect of TbPc₂ SMM on cells should be analyzed experimentally in detail [30]. If the proposed device results in toxicity for *in vivo* environments, then a suitable encapsulation to reduce the effects of toxicity without affecting the resonance and performance should be designed. However, proposed resonators can be utilized for *in vitro* studies, e.g., microfluidic applications, with much more reliability. Effects of biological environment and performance degradation due to eddy currents and coupling with the environment are discussed in detail in [1] where isolating solutions and negligible effects of the environment are assumed.

VI. NANOSCALE AND BIOMEDICAL APPLICATIONS

Exploiting EH, signal carrier generation in the KHz to THz band and modulation capabilities combined with unique properties of graphene and SMMs promise novel applications for *in vivo* biomedical monitoring and sensing in diagnosis and treatment processes. Graphene layers are either resonated by external forces by harvesting vibration energy from biological forces or by various internal mechanisms described in Table I. Non-invasive and continuous EH capabilities combined with ultra-low weight, strong and nanoscale devices promise in-body and wearable applications. Future nanorobotic transceivers can utilize EH for autonomous operation while providing a simple method to modulate data with SWIPT shown in Fig. 1(b) and Table II.

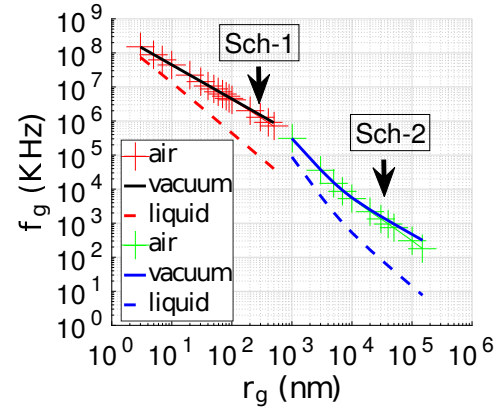


Fig. 6. Resonance frequencies for varying r_g of Sch-1 and Sch-2 type devices.

Cellular level tracking applications such as cancer detection for *in vitro* microfluidic systems can be designed with simple resonators improving current optical methods based on fluorescence, e.g., [29], or magnetic particle based tagging systems. MPI studies are improved by injecting a massive amount of bio-compatible graphene coils, creating waveguides and analyzing induced currents with different frequencies. Mechanisms to exploit proposed system architecture for MPI purposes are left as future works. Capability to generate oscillating magnetic fields, wideband frequency tuning, high signal amplitudes and important mechanical features such as lightweight design, durability and strength promise the utilization of SMMs for such purposes with the resolution determined by the resonator sizes. Graphene is lipophilic making it possible to be used to monitor cellular processes [31]. In addition, THz signal carrier generation can be utilized for non-contact feeding of nanoscale coils by reducing the effects of contact resistances and simplifying the design in [1]. Proposed device promises on-chip THz applications [1].

VII. NUMERICAL ANALYSES

Sch-1 and Sch-2 devices are simulated for varying dimensions of coils and resonator radius. Analysis parameters are summarized in Table III. Resonator radius r_g is chosen between 3 nm and 150 μ m with f_0 between several KHz and hundreds of GHz. Resonator frequencies are shown in Fig. 6 based on detailed model in Section II reaching mmWave frequencies of ≈ 150 GHz for SLG device of the type Sch-1 while covering ultrasound and acoustic frequencies for MLG device of the type Sch-2. Frequency spectrum can be extended with experiments promising THz frequencies theoretically in [26] for high performance MIC and WPT as discussed in [1]. Analyzed acoustic frequencies are validated by theoretical and experimental studies [6].

Resonator thickness h_g is assumed to be either 0.335 nm (SLG) or 30 nm (MLG) in compatible with experimental and theoretical studies with SLG and MLG [6]. Properties of resonators are calculated in Section II while utilizing the constants defined in Table III for TbPc₂ SMM and graphene, i.e., μ_B , g_J , J , ρ , v , E , T_g , t_{ox} and room temperature

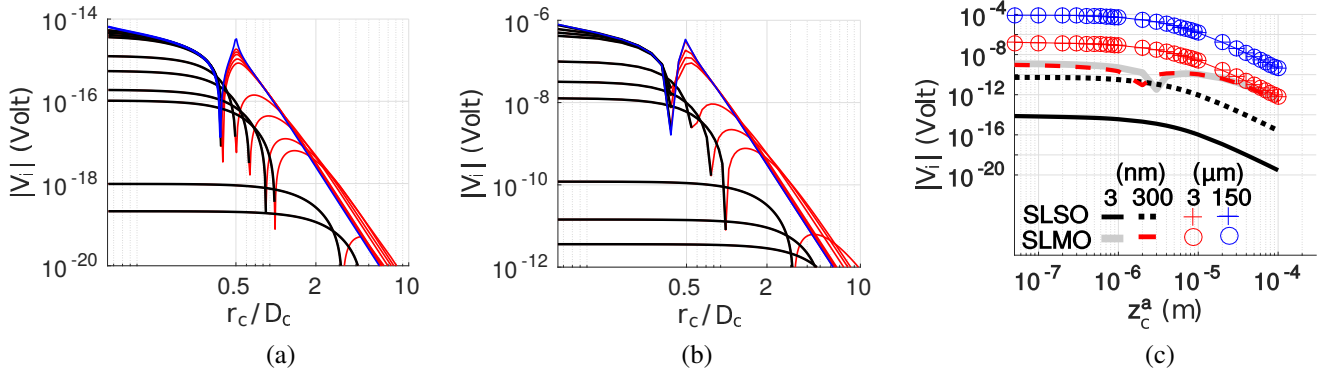


Fig. 7. SLSO performance in air medium for varying r_c with $S_m = 20\%$ and $w = 5 \mu\text{m}$ coil size due to (a) varying z_c^a between 50 nm and 60 μm in Sch-1 with $r_g = 3 \text{ nm}$ and $h_g = 0.335 \text{ nm}$ (SLG), and (b) varying z_c^a between 50 nm and 100 μm in Sch-2 with $r_g = 10 \mu\text{m}$ and $h_g = 30 \text{ nm}$ (MLG). (c) The performance comparison of SLSO and SLMO devices in air where $w = 5 \mu\text{m}$, optimized r_c and $S_m = 20\%$ for varying z_c^a and r_g due to Sch-1 device of $h_g = 0.335 \text{ nm}$ (SLG) with $r_g = 3 \text{ nm}$ and 300 nm and Sch-2 device of $h_g = 30 \text{ nm}$ (MLG) resonators with $r_g = 3 \mu\text{m}$ and 150 μm .

$T = 300 \text{ K}$. $\eta_{SMM} = 0.1$ results in a frequency shift of 5% at most where m_{SMM} , h_{SMM} and a_{SMM} are the weight, height and side length of single TbPc_2 molecule, respectively [32]. They are placed on resonator center with small $k_r = 0.2$. Independent and separated resonators are realized with $k_{\Delta_g} = 1$.

MLMO performance is simulated for varying device parameters and strain levels. d_l is chosen between 1 nm and 1 μm while both the compact layering and more relaxed layering mechanisms are considered, respectively. k_Θ is chosen between 36 and 1800 while analyzing lower thickness and more synchronized layers as k_Θ increases. S_m is analyzed for high level of strain of 20% and lower levels of 1% and $10^{-4}\%$ to analyze harvesting from low power excitations. The noise in the receiver is assumed to be of thermal type with noise spectral density given by $N_{Th} = k_B T$ [1].

Coils are assumed to be made of suspended MLG with intercalation as discussed in detail in [1]. Detailed theoretical modeling of the resistive and capacitive effects of the coil are summarized in the Appendix and in [1] while more accurate modeling with experimental verification is an open issue. Three different coil dimensions are designed for microscale monitoring, MIC and EH purposes, i.e., $w = h = 5, 10$ and $50 \mu\text{m}$, where $a_i = 2 \times k_w \times w = w/5$ and $a_e = a_i + 2 \times w$ with $k_w = 0.1$ for compact dimensions. Single-turn coil ($N_T = 1$) is chosen to have simplification and manufacturing for massive production and placement into biological environments. The cases with $w \geq 10 \times r_g$ is realized with Sch-1 device type to place resonators more compactly with less computational complexity to calculate harvested energy. Otherwise, Sch-2 is utilized with SO centers on a grid. The number of coils is chosen as one with $N_s = 0$ and $k_{\Delta_c} = 1$ to simplify the analysis and to have compact and simple devices. Coils have $\vec{n}_c = [0 \ 0 \ 1]$ for EH purposes at $[x_c \ 0 \ z_c]$ resulting in both vertical displacement $z_c^a \equiv z_c - h/2$ (neglecting oxide thickness t_{ox}) and radial displacement $r_c = \sqrt{x_c^2 + y_c^2} = x_c$.

Contact resistivity of $\rho_c = 10^{-12} \ (\Omega\text{m}^2)$ is assumed based on the promising developments in nanotechnological architectures [1]. The resulting resistance value R_{eff} for the

specific example in Section VII-B is $\approx 22.3 \text{ m}\Omega$ with contact resistance limited regime of $R_c \approx 20 \text{ m}\Omega$ for the compact coil with $w = h = 10 \mu\text{m}$ at $f_0 = 87 \text{ KHz}$. It requires experiments for improving accuracy and verification of the theoretical model [1]. All-graphene architectures with smaller contact resistances promise higher performances.

Three different mediums are considered, i.e., air, liquid or vacuum, with different damping effects to the frequency and different wavelengths of the excitation signal. Two different excitation signals, i.e., acoustic and the one with the speed of light such as optical, are assumed in addition to the electrostatic excitation as shown in Table I. Velocity of the excitation signal is assumed to be $c = 3 \times 10^8 \text{ m/s}$ for Sch-1 devices having the frequencies larger than 10 MHz while the acoustic velocity is assumed to be 343 m/s and 1540 m/s in air and liquid medium, respectively. In the next sections, EH and MIC performances are analyzed.

A. Wireless Energy Harvesting Performances

In the following, SLSO, SLMO and MLMO EH performances are simulated for varying r_g , r_c , $z_c^a > z_{min} = 50 \text{ nm}$, strain level S_m , d_l and k_Θ , and medium.

1) *Single Layer Resonator Performances*: Device performances of SLSO Sch-1 and Sch-2 devices are shown for varying radial and vertical distances with $w = 5 \mu\text{m}$ size single coil in Figs. 7(a) and (b), respectively. It is observed that radial performance drops significantly as r_c is larger than several times D_c (D_c defined as $2a_e$ for side length of the device with $N_s = 0$ instead of Δ_c) for both Sch-1 and Sch-2. Furthermore, as r_c is changed, induced voltage changes sign as shown with different colors. Since SMMs are assumed to reside at the center of the resonator for Sch-2, i.e., for $r_g > r_c$, receiver diversity cannot be utilized efficiently to harvest more energy by placing more coils inside single resonator area.

SLMO performance for z_c^a at an optimized r_c for the maximum induced voltage is shown in Fig. 7(c). As the number of resonators (N_R) increases for Sch-1, performance increases significantly reaching even $\approx 10^5$ improvement for $r_g = 3 \text{ nm}$ resonator and $w = h = 5 \mu\text{m}$ coil dimensions.

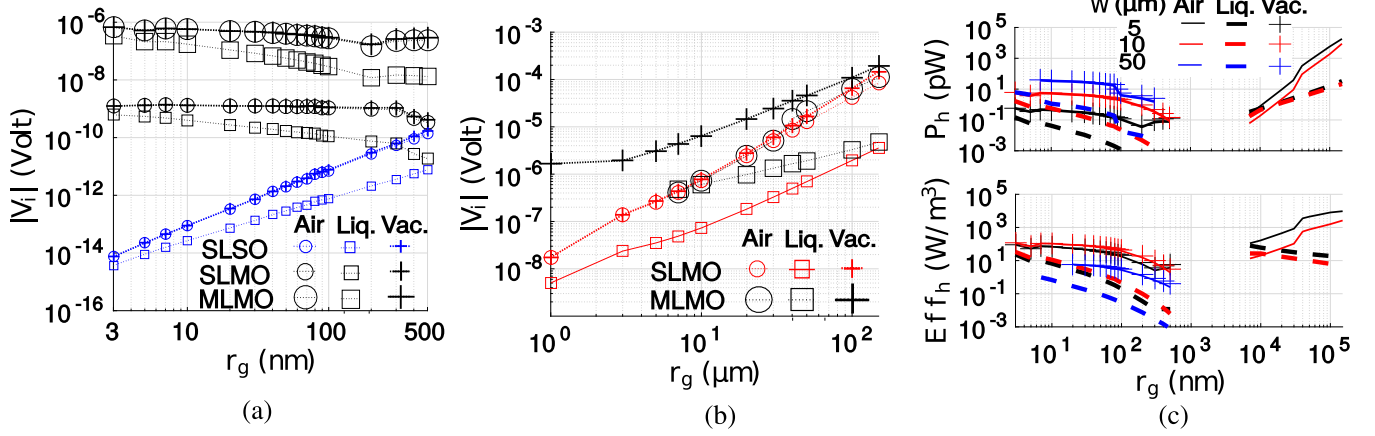


Fig. 8. SLSO, SLMO and MLMO performances with $w = 5 \mu\text{m}$ size single coil for varying r_g and medium where $z_c^a = z_{min}$, $d_l = 1 \text{ nm}$, $k_\theta = 360$, $S_m = 20\%$ and $D_{max} = 50 \mu\text{m}$ showing (a) Sch-1 and (b) Sch-2 type device performances, and (c) their P_h and Eff_h MLMO performances for varying w and the medium.

As the distance is comparable to the several times the coil diameter, the voltage drops with an attenuation constant of almost $\alpha = 4$ in the medium range with $\alpha = 8$ for power, i.e., $P_h \propto |V_i|^2$ as discussed in the Appendix. Sch-1 achieves similar levels of the performance for the same total area as shown in Figs. 7(c) and Fig. 8(a). If it is assumed that the distribution of the radial distance between the coil and resonators are similar due to the significant N_R for large coil area and $\Phi_{z,u}^n$ shows similar values with normalized magnetic moment in (7) then, V_i with SLMO devices for Sch-1 is simplified as approximately proportional to the following:

$$\frac{|V_i|}{|\vec{m}|} \propto N_R N_{SMM} A \omega_0 \quad (13)$$

$$\propto \frac{\Delta_c^2}{r_g^2} \frac{\eta_{SMM} r_g^2 h_g \rho}{m_{SMM}} (\sqrt{S_m} r_g) \frac{1}{r_g} \quad (14)$$

$$= \frac{\Delta_c^2 \eta_{SMM} h_g \rho \sqrt{S_m}}{m_{SMM}} \quad (15)$$

where the radius of total area is proportional to Δ_c , $A \propto \sqrt{S_m} r_g$ and $\omega_0 \propto 1/r_g$ for SLG.

2) *Multi-layer Resonator Performances:* In Figs. 8(a) and (b), comparison among SLSO, SLMO and MLMO devices are shown in various medium of air, liquid and vacuum. The other parameters are $d_l = 1 \text{ nm}$, $z_c^a = 50 \text{ nm}$, $k_\theta = 360$ for highly synchronized resonating layers, $S_m = 20\%$ and $D_{max} = 50 \mu\text{m}$ suitable for microscale applications. As shown in Fig. 8(a), MLMO significantly improves SLMO performance for all medium types reaching $\approx 10^3$ times improvement while $\approx 10^8$ for SLSO. A similar improvement is observed for large resonator sizes with the improvement vanishing as the number of layers decreases (increasing r_g) as shown in Fig. 8(b). Sch-2 performances are higher than Sch-1 replacing Δ_c^2 in (15) with increasing r_g^2 . Furthermore, liquid leads to lower operating frequency and performance.

In Fig. 8(c), it is observed that tens of pW level powers are harvested including mmWave frequencies around 150 GHz while tens of nWs power can be harvested at acoustic frequencies with larger resonators of tens of micrometer radius

(with the corresponding frequencies in Fig. 6). Eff_h (W/m^3) reaches several hundreds at mmWave frequencies to orders of 10^4 at acoustic and ultrasound frequencies with a significant nanoscale EH performance. These results are comparable with state of the art triboelectric harvesters with efficiencies on the order of 10^4 (W/m^3) in [33] but with much smaller sizes to be embedded in nano-biological units. Simplicity of manufacturing, planar structure and MI based applications are other advantages. An upper bound of EH is provided for electromagnetic harvesters with $1.9 \cdot 10^{-6} V_r^2 f_0^2$ in [11] where V_r is in cm^3 and f_0 is in Hz. This results in 17.5 nW for $r_g = 100 \mu\text{m}$, $w = h = 5 \mu\text{m}$, $z_c^a = 50 \text{ nm}$, $f_0 \approx 300 \text{ KHz}$ and in air medium where the dimensions of the optimum efficiency device is $\approx 200 \mu\text{m} \times 200 \mu\text{m} \times 8 \mu\text{m}$. The proposed device has the maximum peak power of $\approx 5.7 \text{ nW}$ as shown in Fig. 8(c) comparable with the maximum state of the art generators although exact dimensions should include storage units such as supercapacitors to make a more fair comparison.

D_T^{max} , D_{max} and D_S , and the numbers of SMMs, resonators and layers in SLSO, SLMO and MLMO devices are shown in Figs. 9(a) and (b), respectively. D_T^{max} of Sch-1 with small r_g is similar for varying medium as shown in Fig. 9(a). The number of layers is increased for Sch-2 with respect to $\min\{D_T^{max}/D_S, D_{max}/D_S\}$ in water and in air with increasing D_T^{max} . D_S values are smaller than $\approx 20 \mu\text{m}$ suitable to be placed into nanoscale units. In addition, number of resonators with the smallest r_g reaches $\approx 10^7$ for Sch-1 while it succeeds to have an approximately constant number of SMMs and layers for small r_g due to dependency in (15) and minor increase in D_S in Fig. 9(b). Number of SMMs reaches to the orders of 10^{10} and 10^{11} for Sch-1 and Sch-2, respectively, while the number of layers is smaller than ≈ 2000 and 2 for Sch-1 and Sch-2 devices, respectively, in air.

3) *Effects of Phase Synchronization, Interlayer Distance and Strain:* The relation between D_T^{max} and D_S , and V_i performance for varying k_θ are shown in Figs. 9(c) and (d), respectively, for $w = 10 \mu\text{m}$ coil, $z_c^a = z_{min}$, $S_m = 20\%$ and $d_l = 1 \text{ nm}$ in vacuum. It is observed that as k_θ increases D_T^{max} decreases while the decrease changes the total number

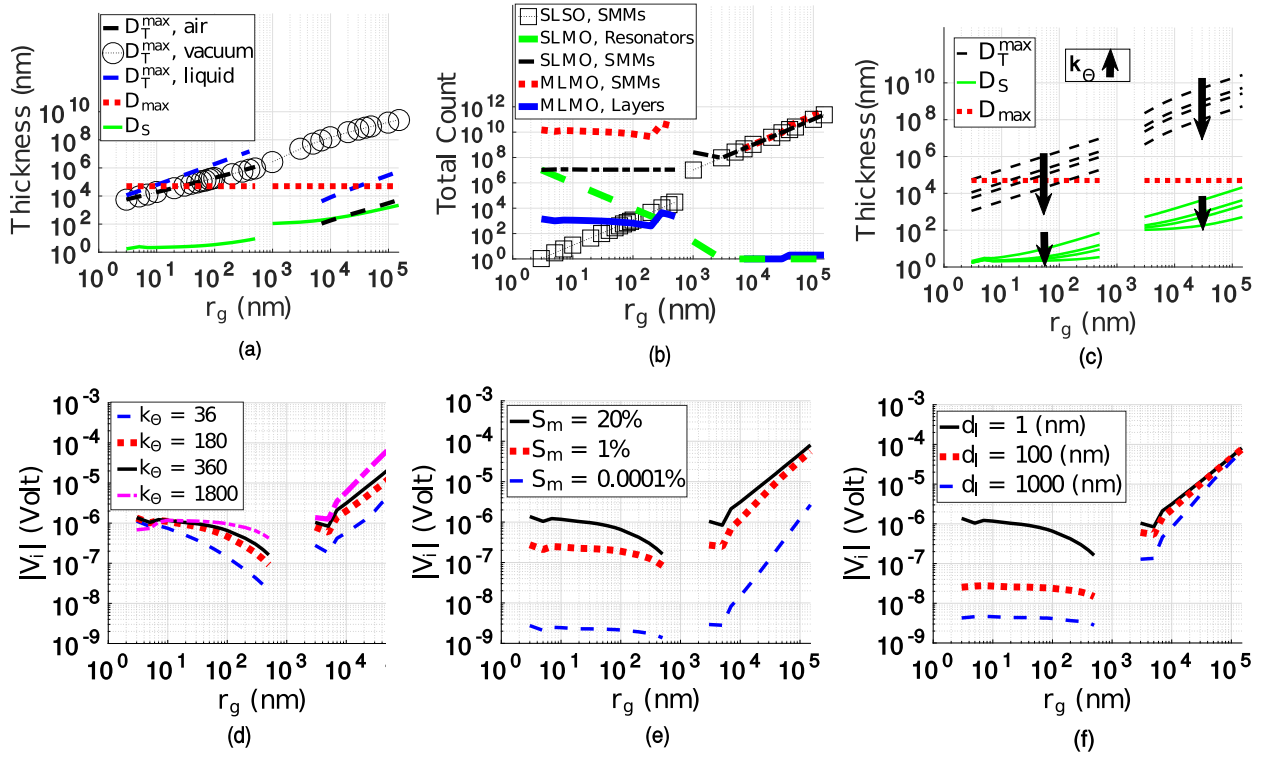


Fig. 9. (a) D_T^{max} , D_{max} and single layer thickness D_S for varying medium and r_g , and (b) total counts of SMMs, layers and resonators in air for varying r_g where SLSO, SLMO and MLMO devices have $w = 5 \mu\text{m}$, $z_c^a = z_{min}$, $d_l = 1 \text{ nm}$, $k_\theta = 360$, $S_m = 20\%$ and $D_{max} = 50 \mu\text{m}$. (c) Bounding and single layer thicknesses, and (d) $|V_i|$ in vacuum with $w = 10 \mu\text{m}$, $d_l = 1 \text{ nm}$, $S_m = 20\%$ and $z_c^a = z_{min}$ for varying k_θ and r_g . $|V_i|$ in vacuum with $w = 10 \mu\text{m}$, $k_\theta = 360$ and $z_c^a = z_{min}$ (e) for varying S_m and r_g with $d_l = 1 \text{ nm}$ and, (f) for varying d_l and r_g with $S_m = 20\%$.

of layers more for longer resonator radius. However, total thickness is becoming lower than D_{max} limiting the number of layers for small r_g as shown in Fig. 9(c). Performance improvement is observed for both Sch-1 and Sch-2 bounded by $\min\{D_T^{max}/D_S, D_{max}/D_S\}$ as shown in Fig. 9(d) while improvement is more clearly observed for larger radius Sch-1 resonators. Effect of d_l is similar to k_θ changing the number of layers and performance especially on Sch-1 with SLG layers as shown in Fig. 9(f). However, effect of strain is different such that increasing number of layers due to low strain cannot overwhelm the reduction due to lower vibration amplitude as shown in Fig. 9(e).

B. Wireless Communications Channel Performance

Received power in a single coil due to MLMO resonators is expressed as $P_h = |V_i|^2 / (8 R_{eff})$ as discussed in the Appendix. If we assume the receiver operates in the thermal noise limited regime and a low data rate monitoring is realized by detecting the oscillation frequency of SMMs with tuned coil receivers, then SNR at the frequency ω is expressed as $SNR = P_h / N_{Th} B$ where B denotes ultra-narrow bandwidth of the resonator. The channel geometry provided in Fig. 2(b) is analyzed for varying r_c , z_c^a and r_g where $B = 10 \text{ Hz}$ and $w = 10 \mu\text{m}$. The ultra-narrow bandwidth allows low data rate communications while the limit to lower the bandwidth depends on the excitation source or the mechanical effects. If frequency tagging is utilized, then different resonators are placed or attached with target units, e.g., cells or nano-robots,

and they are tracked based on the detection of the frequency at distances of several millimeters providing a novel framework for future nanoscale MPI or tracking applications.

Performances without angular misalignments of MLMO devices for varying vertical and radial distances are shown in Fig. 10(a) for liquid medium with $w = 10 \mu\text{m}$, $r_g = 30 \mu\text{m}$, $f_0 \approx 87.4 \text{ KHz}$ and $B = 10 \text{ Hz}$. Performance decrease for varying z_c^a with small r_c is limited to 3 dB for $r_c \leq 5 \mu\text{m}$ while the drop at small z_c^a is significantly high for larger r_c . It is possible to have zero SNR level for hundreds of micrometer vertical distances with smaller effect of varying r_c . In [1], the effects of angular misalignments on MI waveguide channels extending ranges significantly are discussed emphasizing the robustness to small angular disorientations less than $\pi/3$ for radial displacements less than 2.5 times the coil radius. Numerical analysis for angular misalignments is left as a future work in a more complicated relaying waveguide scheme.

Performance for varying r_g is shown in Fig. 10(b) with the same medium, coil size and bandwidth parameters. SNR drop is $\approx 80 \text{ dB}$ per decade while it is possible to receive larger than zero SNR at distances reaching $400 \mu\text{m}$ for mmWave frequencies and hundreds of micrometer distances for acoustic and ultrasound frequencies.

As a future work, the effect of passive coils within a waveguide structure will be analyzed to improve the range to much longer distances including macroscale ranges as discussed in [1]. As the number of units attached with coils increases, they perform as waveguides for the resonating SMMs potentially

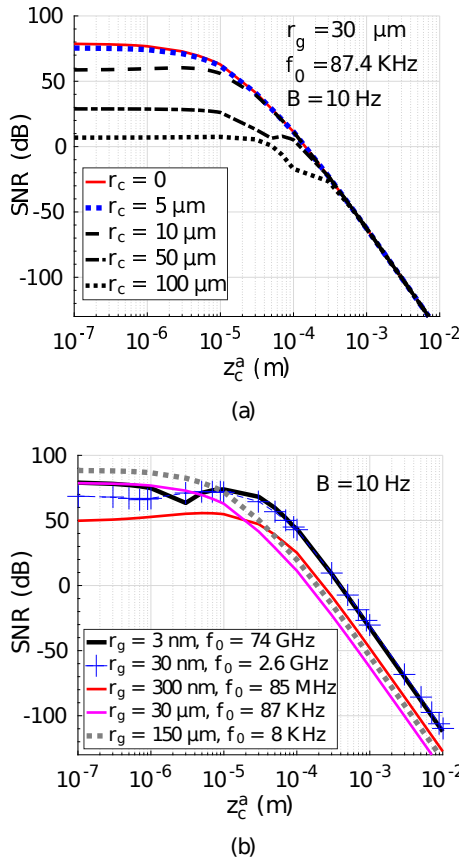


Fig. 10. SNR performances of MLMO devices in liquid (a) for varying r_c and z_c^a with $r_g = 30 \mu\text{m}$, and (b) for varying r_g and z_c^a at $r_c = 0$, where $w = 10 \mu\text{m}$, $S_m = 20\%$, $d_l = 1 \text{ nm}$ and $k_\Theta = 360$.

allowing a *waveguide relaying network* to carry the signals to the external receivers. Resonators can be embedded into nanoscale communication networks and biological units, e.g., cells or similar microscale volumes to track or identify them at millimeter ranges. Waveguide scheme provides a novel form of MPI application with cellular resolution. A low cost architecture can be achieved for simultaneous multi-cell tracking applications. Performance analyses of waveguides, angular orientations and densities of resonators are open issues.

VIII. CONCLUSION

In this article, graphene nanoscale resonators are combined with SMMs to realize nanoscale EH, MIC and WPT simultaneously by exploiting unique mechanical and geometrical advantages of graphene with high and stable orbital magnetic moment of TbPc_2 SMM grafted on graphene. Low complexity mechanical design supports novel modulation methods achieving SWIPT with real-time carrier signal generation in the KHz to THz band. Numerical analysis presents tens of nanowatts power EH and efficiencies of 10^4 W/m^3 in acoustic and ultrasound frequencies as nanoscale and high frequency alternatives to state of the art electromagnetic vibrational EH devices. Challenges to realize system prototype are discussed. Proposed system design promises applications in the near future such as nanoscale tagging of biological structures,

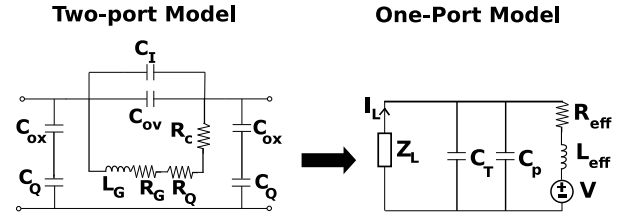


Fig. 11. Two-port model of graphene OC inductor and circuit theoretical modeling of WG with one-port coil models [1].

biomedical sensing and communications, EH and modulation for nano-robotic transceivers and MPI systems.

APPENDIX

The equivalent circuit model is defined in detail in [1]. $C_{ov} = \epsilon_{r,ox} \epsilon_0 A_o / h_{ov}$ where $A_o = N_T w^2$, N_T is the number of turns, $h_{ov} \equiv t_{ox} / 2$, $\epsilon_0 = 8.854 \times 10^{-12} \text{ (F/m)}$ and $\epsilon_{r,ox} = 3.9$ are absolute vacuum and relative oxide permittivity values, respectively. Furthermore, C_{ox} is approximated with distributed capacitance modeling for graphene while C_I is neglected due to $N_T = 1$ [1]. C_Q equals to $N_{ch} N_L 4 q^2 / (h_p v_F)$ where $h_p = 6.626 \times 10^{-34} \text{ (J} \times \text{s)}$ is Planck's constant, q is electron charge, $N_L = h / s_L$ is the number of single layers, $s_L = 0.575 \text{ nm}$, N_{ch} is the number of conducting channels in one layer given by $\sum_{j=0}^{n_c} (1 + e^{(E_j - E_F) / k_B T})^{-1} + \sum_{j=0}^{n_v} (1 + e^{(E_j + E_F) / k_B T})^{-1}$ where $E_j = j h_p v_F / 2 w$ assuming metallic graphene, $v_F \approx 8 \times 10^5 \text{ m/s}$ is the Fermi velocity and $E_F = 0.6 \text{ eV}$. Parameters shown in Fig. 11 are obtained as $C_p = C_I + C_{ov} + (1/C_{ox} + 1/C_Q)^{-1}$ and $R_{eff} = R(\omega) + R_Q + R_c$ where $\omega = 2 \pi f$, $L_{eff} = L(\omega)$, $R(\omega)$ and $L(\omega)$ are equivalent resistance and inductance, respectively, $R_c = 2 \rho_c / (w h)$, ρ_c is the contact resistivity in $(\Omega \text{ m}^2)$ and $R_Q = h_p / (2 q^2 N_{ch} N_L)$ [1]. Then, the tuning capacitor C_T and the matched load $Z_L = R_L + j X_L$ result in $P_h = |V_p|^2 / (8 R_{eff})$ at ω and V_p equals to V_{z_c, r_c}^{MLMOc} and V_{z_c, i_y}^{MLMOc} for Sch-1 and Sch-2, respectively.

ACKNOWLEDGEMENT

The authors thank to Dr. Gorkem Memisoglu and the support of Vestel Electronics.

REFERENCES

- [1] B. Gulbahar, "Theoretical analysis of magneto-inductive THz wireless communications and power transfer with multi-layer graphene nano-coils," *IEEE Trans. on Molecular, Biological, and Multi-Scale Comms.*, vol. 3, no. 1, pp. 60–70, 2017.
- [2] X. Hu, K. Aggarwal, M.X. Yang, K.B. Parizi, X. Xu, D. Akin, A.S. Poon and H.S.P. Wong, "Micrometer-scale magnetic-resonance-coupled radio-frequency identification and transceivers for wireless sensors in cells", *Physical Review Applied*, vol. 8, no. 1, pp. 014031-1–014031-13, 2017.
- [3] A. Candini et al., "Graphene spintronic devices with molecular nanomagnets," *Nano Lett.*, vol. 11, no. 7, p. 2634, 2011.
- [4] L. Bogani and W. Wernsdorfer, "Molecular spintronics using single-molecule magnets", *Nature Materials*, vol. 7, no. 3, pp. 179–186, 2008.
- [5] Q. Zhou et al., "Graphene electrostatic microphone and ultrasonic radio," *Proceedings of the National Academy of Sciences*, vol. 112, no. 29, pp. 8942–8946, 2015.

- [6] A. Castallanos-Gomez et al., "Mechanics of freely suspended ultrathin layered materials," *Annalen der Physik*, vol. 527, no. 1-2, pp. 27–44, 2015.
- [7] C. Cervetti et al., "The classical and quantum dynamics of molecular spins on graphene," *Nature Materials*, vol. 15, no. 2, pp. 164–168, 2016.
- [8] M. Ganzhorn et al., "Carbon nanotube nanoelectromechanical systems as magnetometers for single-molecule magnets," *ACS Nano*, vol. 7, no. 7, pp. 6225–6236, 2013.
- [9] B. Lassagne, D. Ugnati and M. Respaud, "Ultrasensitive magnetometers based on carbon-nanotube mechanical resonators," *Physical Review Letters*, vol. 107, no. 13, pp. 130801-1–130801-5, 2011.
- [10] L. Gragnaniello et al., "Uniaxial 2D superlattice of Fe₄ molecular magnets on graphene," *Nano Letters*, vol. 17, no. 12, pp. 7177–7182, 2017.
- [11] S. D. Moss et al., "Scaling and power density metrics of electromagnetic vibration energy harvesting devices," *Smart Materials and Structures*, vol. 24, no. 2, p. 023001, 2015.
- [12] E. Asadi, H. Askari, M. Behrad Khamesee, A. Khajepour, "High Frequency Nano Electromagnetic Self-Powered Mass Sensor: Concept, Modelling and Analysis," *Measurement*, 2017.
- [13] Y. Zi, and Z. L. Wang, "Nanogenerators: An emerging technology towards nanoenergy," *APL Materials*, vol. 5, no. 7, p. 074103, 2017.
- [14] E. Y. Yu et al., "Magnetic particle imaging: a novel in vivo imaging platform for cancer detection," *Nano Letters*, vol. 17, no. 3, pp. 1648–1654, 2017.
- [15] B. Gulbahar, "Network topology modulation for energy and data transmission in Internet of magneto-inductive things," *Proc. of IEEE GLOBECOM 2016 First Int. Workshop on the Internet of Everything*, USA, pp. 1–6, 2016.
- [16] R. Baltic et al., "Superlattice of single atom magnets on graphene," *Nano Letters*, vol. 16, no. 16, 2016.
- [17] Q. Zhou et al., "Graphene electrostatic microphone and ultrasonic radio," *Proceedings of the National Academy of Sciences*, vol. 112, no. 29, pp. 8942–8946, 2015.
- [18] X. S. Bunch et al., "Stamp transferred suspended graphene mechanical resonators for radio frequency electrical readout," *Nano Letters*, vol. 12, no. 1, pp. 198–202, 2011.
- [19] S. H. Mousavi, P. T. Rakich, Z. Wang, "Strong THz and infrared optical forces on a suspended single-layer graphene sheet," *ACS Photonics*, vol. 1, no. 11, pp. 1107–1115, 2014.
- [20] J. S. Bunch et al., "Impermeable atomic membranes from graphene sheets," *Nano Lett.*, vol. 8, no. 8, p. 2458, 2008.
- [21] C. L. Wong et al., "Characterization of nanomechanical graphene drum structures," *Journal of Micromechanics and Microengineering*, vol. 20, no. 11, p. 115029, 2010.
- [22] M. Yu and B. Balachandran, "Sensor diaphragm under initial tension: linear analysis," *Experimental Mechanics*, vol. 45, no. 2, pp. 123–129, 2005.
- [23] B. Gulbahar and G. Memisoglu, "Nanoscale optical communications modulator and acousto-optic transduction with vibrating graphene and resonance energy transfer," *Proc. of The IEEE ICC 2017 Selected Areas in Communications Symposium Molecular, Biological, and Multi-Scale Communications Track*, 21-25 May, Paris, France, 2017.
- [24] C. X. Zhao, W. Xu, F. M. Peeters., "Cerenkov emission of terahertz acoustic-phonons from graphene," *Applied Physics Letters*, vol. 102, no. 22, p. 222101, 2013.
- [25] Y.E. Chenran et al., "λ-size ITO and graphene-based electro-optic modulators on SOI," *IEEE Journal of Selected Topics in Quantum Electronics*, vol. 20, no. 4, pp. 40–49, 2014.
- [26] A. S. Tsiamaki, S. K. Georgantzinis, N. K. Anifantis, "Monolayer graphene resonators for mass detection: a structural mechanics feasibility study," *Sensors and Actuators A: Physical*, vol. 217, pp. 29–38, 2014.
- [27] J. D. Rinehart, J. R. Long, "Exploiting single-ion anisotropy in the design of f-element single-molecule magnets," *Chemical Science*, vol. 2, no. 11, pp. 2078–2085, 2011.
- [28] A.J. Sneller and B.P. Mann, "On the nonlinear electromagnetic coupling between a coil and an oscillating magnet," *Journal of Physics D: Applied Physics*, vol. 43, no. 29, p. 295005, 2010.
- [29] B. Gulbahar and G. Memisoglu, "CSSTag: Optical nanoscale radar and particle tracking for in-body and microfluidic systems with vibrating graphene and resonance energy transfer," *IEEE Trans. on NanoBio-science*, vol. 16, no. 8, pp. 905–916, 2017.
- [30] K. T. Rim et al., "Toxicological evaluations of rare earths and their health impacts to workers: a literature review," *Safety and Health at Work*, vol. 4, no. 1, pp. 12–26, 2013.
- [31] K. S. Novoselov et al., "A roadmap for graphene," *Nature*, vol. 490, no. 7419, pp. 192–200, 2012.
- [32] S. Stepanow et al., "Spin and orbital magnetic moment anisotropies of monodispersed bis (phthalocyaninato) terbium on a copper surface," *Journal of the American Chemical Society*, vol. 132, no. 34, pp. 11900–11901, 2010.
- [33] P. Bai et al., "Integrated multilayered triboelectric nanogenerator for harvesting biomechanical energy from human motions," *ACS Nano*, vol. 7, no. 4, pp. 3713–3719, 2013.